



# High-spin state Fe(III) doped TiO<sub>2</sub> for electrocatalytic nitrogen fixation induced by surface F modification

Guangxin Song<sup>a,1</sup>, Rui Gao<sup>a,b,1</sup>, Zhao Zhao<sup>a,\*,1</sup>, Yujun Zhang<sup>c</sup>, Huaqiao Tan<sup>d</sup>, Haibo Li<sup>a</sup>, Dandan Wang<sup>a,\*</sup>, Zaicheng Sun<sup>e,\*</sup>, Ming Feng<sup>a,\*</sup>

<sup>a</sup> Key Laboratory of Functional Materials Physics and Chemistry of the Ministry of Education, Jilin Normal University, Changchun 130103, PR China

<sup>b</sup> Department of Chemical Engineering, University of Waterloo, 200 University Avenue West, Waterloo, Ontario N2L 3G1, Canada

<sup>c</sup> Institute of High Energy Physics, Chinese Academy of Sciences, Yuquan Road 19B, Shijingshan District, Beijing 100049, PR China

<sup>d</sup> Key Laboratory of Polyoxometalate Science of Ministry of Education, Faculty of Chemistry, Northeast Normal University, Changchun 130103, PR China

<sup>e</sup> Center of Excellence for Environmental Safety and Biological Effects, Beijing Key Lab for Green Catalysis and Separation, Department of Chemistry and Chemical Engineering, College of Environmental and Energy Engineering, Beijing University of Technology, 100 Pingleyuan, Beijing 100124, PR China

## ARTICLE INFO

### Keywords:

Electrocatalysis

N<sub>2</sub> Fixation

Surface fluorine treatment

Iron doping

Surface electronic state manipulation

## ABSTRACT

It is a challenging task to overcome the bottleneck of N<sub>2</sub> adsorption and activation in N<sub>2</sub> reduction reaction (NRR). Regulating the catalyst surface electronic state is treated as a potential strategy to prevail over the barrier. Here, incorporating Fe as a dopant in the TiO<sub>2</sub> nanoparticles can generate oxygen vacancies and dopant energy levels, promoting the adsorption and activation of N<sub>2</sub> molecules. F surface modification induces Fe (III) in the high spin state and upshifts the dopant energy level. That facilitates Fe 3d electrons backdonation to N 1π\* orbital promotes the activation of N<sub>2</sub> molecule and reduces the limiting potential of NRR. Therefore, F-Fe: TiO<sub>2</sub> electrocatalyst achieved the highest Faradaic efficiency and maximum NH<sub>3</sub> production rate of 27.67% and 27.86 μg h<sup>-1</sup> mg<sub>cat</sub><sup>-1</sup> at -0.5 V v.s. reversible hydrogen electrode. This work provides deep insights into the design surface electronic state of catalyst toward efficient N<sub>2</sub> to NH<sub>3</sub> conversion.

## 1. Introduction

Synthetic ammonia (NH<sub>3</sub>) is a key synthetic chemical precursor for agriculture fertilizers that has revolutionized the food supply and is also a promising non-carbon-based energy carrier in response to the imminent fossil energy crisis [1,2]. To date, the commercial ammonia synthesis is dominated by the Haber-Bosch process, which usually operated under harsh conditions (200–350 atm, and 400–550 °C) because of the extremely inert N≡N bond dissociation energy (940.95 kJ mol<sup>-1</sup>) [3,4]. The corresponding ammonia industry consumes ca. 1–3% of global energy supply and accounts for ca. 1.6–3% global fossil fuel-derived CO<sub>2</sub> emissions annually [5,6]. Therefore, the development of an energy-efficient alternative route under milder operating conditions is highly important and desired of ongoing chemistry and catalysis research [7–9].

Electrochemical N<sub>2</sub> reduction reaction (eNRR) offers a promising alternative route [10,11]. So far, state-of-the-art NRR electrocatalysts are noble metal catalysts, such as Au, Rh, Pd, and Ru, owing to the

suitable electronic structure and high electrical conductivity [12–15]. Since the high cost limits their practical application, it is of prime meaning to develop noble-metal-free highly efficient NRR electrocatalysts [16,17]. Remarkably, 3d transition metal-based oxides (TMOs) are considered promising candidate electrocatalysts due to their unique electronic structures and natural abundance [18]. Among them, TiO<sub>2</sub> based catalysts have been demonstrated to be an effective and good activity for the NRR in recent studies. Iron (Fe) with unpaired electrons in 3d orbitals, as a primary element of biological nitrogenases in nature and a catalyst of the Haber-Bosch process, helps in strong adsorption to N<sub>2</sub> by forming the Fe-N bond. Different valance state of Fe is beneficial to generate oxygen vacancies. The hybridization of 3d orbitals in the interaction of Ti and Fe can also induce a dopant energy level in the bandgap, facilitating the electron migration to the N-related intermediate species absorbed on active sites [19]. Fang et al. predicted the active site with a high spin magnetic moment is beneficial to reducing the limiting potential of eNRR [20]. To achieve high spin Fe(III), the “fluorine effect” has been extensively investigated, due to the strong

\* Corresponding authors.

E-mail addresses: [rbzhao2003@qq.com](mailto:rbzhao2003@qq.com) (Z. Zhao), [mila880227@126.com](mailto:mila880227@126.com) (D. Wang), [sunzc@bjut.edu.cn](mailto:sunzc@bjut.edu.cn) (Z. Sun), [mingfeng@jlnu.edu.cn](mailto:mingfeng@jlnu.edu.cn) (M. Feng).

<sup>1</sup> These authors contributed equally

complexation between F and 3d transition metals and the high electronegativity of fluorine [21]. The 3d orbital of surface Fe and the 2p orbital of surface bridging F were inevitably hybridized, resulting in emerging surface states [22]. The introduction of fluorine can easily occupy the surface oxygen vacancies, thereby increasing the asymmetry of the coordination environment to iron atoms. Therefore, surface fluoride modification can provide an excellent platform for investigating the role of iron dopants in  $\text{TiO}_2$  in regulating the surface electronic state, which is the key factor to achieve transformative advances toward enhanced the electron backdonation to the adsorbed  $\text{N}_2$  molecule [23].

Inspiration the above, we proposed the following strategy: Fe-doped  $\text{TiO}_2$  (Fe:  $\text{TiO}_2$ ) is synthesized via the simple sol-gel method and followed by introducing fluorine modification by NaF treatment for boosting electrocatalytic NRR performance. The advantages of this strategy are: I) the incorporation of Fe dopant creates defect energy level and oxygen vacancies served as active sites. II) F strongly attracts the electron cloud resulting in that Fe is closer to ferric ion ( $\text{Fe}^{3+}$ ) due to the largest electronegativity. III) Ferric ion induces the defective energy level upshifting, increasing the driven force the transition from trap state to the antibonding  $1\pi_g^*$  orbital of adsorbed  $\text{N}_2$  ( $^*\text{N}_2$ ). IV) The electron in the  $e_g$  orbital weakens the bonding strength of the N-N bond owing to regulating the spin-state of the surface ferric ion by the Kondo effect [24]. Based on the experimental results and theoretical calculations, synergistic interaction between Fe and F on the surface of Fe:  $\text{TiO}_2$  promotes  $\text{N}_2$  adsorption and activation while facilitating electron backdonation and consequently lower the energy barrier of the rate-limiting step. The optimal F-Fe:  $\text{TiO}_2$  electrocatalyst achieved the highest faradaic efficiency (FE) and maximum  $\text{NH}_3$  production rate of 27.67% and  $27.86 \mu\text{g h}^{-1} \text{mg}_{\text{cat}}^{-1}$  at  $-0.5 \text{ V}$  versus reversible hydrogen electrode (versus RHE). we demonstrated a general methodology to achieve efficient ammonia synthesis performance through doping heteroatoms and manipulating surface electronic states.

## 2. Experimental

### 2.1. Synthesis of Fe doped $\text{TiO}_2$

Fe doped  $\text{TiO}_2$  nanoparticles (Fe:  $\text{TiO}_2$ ) were synthesized by using a sol-gel method. Firstly, to dissolved 1.6 g of F127 and a certain percentage of ferric chloride in 30 mL of ethanol solvent and stirred for 1 h at  $60^\circ\text{C}$ , added 3.5 mL TBT, 2.3 mL of acetic acid, and 0.7 mL of hydrochloric acid, stirred at room temperature for 30 min. Then, the mixed solution was transferred to a blast drying oven and dried at  $60^\circ\text{C}$  for 24 h to obtain a Fe:  $\text{TiO}_2$  sol-gel. Subsequently, the Fe:  $\text{TiO}_2$  sol-gel was milled and sintered at  $450^\circ\text{C}$  for 4 h in a muffle furnace to get the Fe:  $\text{TiO}_2$  powder.

### 2.2. Synthesis of F-Fe doped $\text{TiO}_2$

As for surface fluorine treatment, as-prepared Fe:  $\text{TiO}_2$  was used as the original substrate. Briefly, Fe:  $\text{TiO}_2$  was immersed in a solution containing 0.05 M NaF for 20 min F-Fe:  $\text{TiO}_2$  with different amounts of F was treated with 0.01 M, 0.05 M, and 0.1 M NaF for 20 min. Then, the treated Fe:  $\text{TiO}_2$  nanoparticles were directly annealed at  $400^\circ\text{C}$  for 3 h.

### 2.3. Preparation of F-Fe: $\text{TiO}_2$ /CP electrode

Carbon paper (CP) was cleaned via brief sonication with ethanol and water several times. To prepare the Fe:  $\text{TiO}_2$  ink, 5 mg F-Fe:  $\text{TiO}_2$  and 120  $\mu\text{L}$  5 wt% Nafion solution were dispersed in 1 mL ethanol followed by 2 h sonication to form a homogeneous ink. Then, 20  $\mu\text{L}$  ink was loaded onto the CP ( $1 \times 1 \text{ cm}^2$ ) and dried under ambient conditions.

## 3. Results and discussion

### 3.1. Electrocatalyst synthesis and characterization

Typically, the pore-forming additive (F127),  $\text{FeCl}_3$ , and tetrabutyl titanate (TBT) were hydrolyzed in a water and ethanol solution. The as-prepared gel was washed, dried, and calcined at  $400^\circ\text{C}$  for 3 h to form mesoporous Fe-doped  $\text{TiO}_2$  NPs (Fe:  $\text{TiO}_2$ ). Subsequently, the Fe:  $\text{TiO}_2$  NPs were dispersed in a certain amount of NaF aqueous solution under magnetic stirring for 1 h and followed annealing in the air to prepare the F modified Fe:  $\text{TiO}_2$  (F-Fe:  $\text{TiO}_2$ ). The detailed experimental procedures see the Supporting information. The powder X-ray diffraction (XRD, Fig. 1A) patterns disclose that all the samples are identified with the peaks of anatase  $\text{TiO}_2$  (PDF No.89-4921). No characteristic peak of iron oxides was observed, implying that no large-sized crystalline iron oxide is formed. Considering the similar atomic radii of Fe atom and Ti atom, a series of Fe:  $\text{TiO}_2$  NPs with various Fe values were compared in Fig. S1. No obvious peak shift and a slightly broader diffraction peak indicate heteroatom Fe does not change the crystalline phase but form slightly poor crystal quality. In addition, no patterns changing are observed even after the varying amount fluoride treatments (Fig. S2), these results further confirm that there is no residue of fluoride.

Both scanning electron microscopy (SEM) and transmission electron microscopy (TEM) were used for in-depth study of the morphology and composition of samples. SEM images reveal that mesoporous  $\text{TiO}_2$  has a nanoparticle-aggregates structure (Fig. S3A). After doping with Fe and fluoride treatment, the morphology remains unchanged (Fig. S3B and S3C). TEM images and High-resolution (HR)-TEM images of prepared samples were also given in Fig. 1B and Fig. S4-S6. The diameter of the nanoparticles is mostly less than 20 nm. Only one lattice fringe of 0.35 nm corresponding to (101) of  $\text{TiO}_2$  was observed in HR-TEM images, which were consistent in apparent morphology indicating Fe doping and fluorination do not change the size of the nanoparticles and the crystal phase (Fig. 1C). In addition, it is known that the smaller size inevitably leads to a larger specific surface area, which is an important factor in the improvement of catalytic activity. The  $\text{N}_2$  sorption isotherm results (Fig. S7) showed a typical type IV H1 hysteresis loop with a high surface area. Table S1 presents the Brunauer-Emmett-Teller (BET) specific surface area values (ca.  $100 \pm 12 \text{ m}^2 \text{g}^{-1}$ ) of  $\text{TiO}_2$ , Fe:  $\text{TiO}_2$ -X, and X-F-Fe:  $\text{TiO}_2$  samples, illustrating that the incorporation of Fe atoms or surface fluorination had little effect on the specific surface area of  $\text{TiO}_2$ . Furthermore, the elemental energy-dispersive X-ray spectroscopy (EDS) elemental mapping (Fig. 1D-1H, S8) was employed to confirm the distribution of Fe heteroatom and the presence of fluorine at the surface. The results reveal that Fe and F elements are uniformly distributed over the entire nanoparticles without any aggregation. To further confirm the contents of trace elements the inductively-coupled plasma mass spectroscopy (ICP-MS) was employed, the results of element analysis revealed that the ratio of Fe to Ti is consistent with the feed ratio, and no significant differences after the fluoride treatment were evident (Table S2).

Fig. 1I presented the Diffuse reflectance spectroscopy (DRS) UV-vis absorption spectra of  $\text{TiO}_2$ , Fe:  $\text{TiO}_2$ , and F-Fe:  $\text{TiO}_2$  samples. It can be seen that the pure  $\text{TiO}_2$  sample displayed intrinsic absorption peaks in the ultraviolet area, whereas Fe:  $\text{TiO}_2$  and F-Fe:  $\text{TiO}_2$  samples showed a redshift of absorbing edge. Based on the corresponding Tauc plots (Fig. 1J) converted from the UV-vis DRS absorption spectra, the  $E_g$  of  $\text{TiO}_2$ , Fe:  $\text{TiO}_2$ , and F-Fe:  $\text{TiO}_2$  is evaluated to be 3.18 eV, 2.56 eV, and 2.52 eV respectively. With the increasing Fe doping amounts, the color of Fe:  $\text{TiO}_2$ -X evolves from white to orange, which is consistent with the UV-vis spectra (Fig. S9). However, with the adjusting fluorination amounts, no significant reduction in the spectral absorption was found compared with Fe:  $\text{TiO}_2$  (Fig. S10). The first absorption came from the electrons excited from the valence band to the conduction band, the observed absorption shifted to the visible region appeared as a result of the orbital hybridization of the Fe 3d in the crystalline environment of

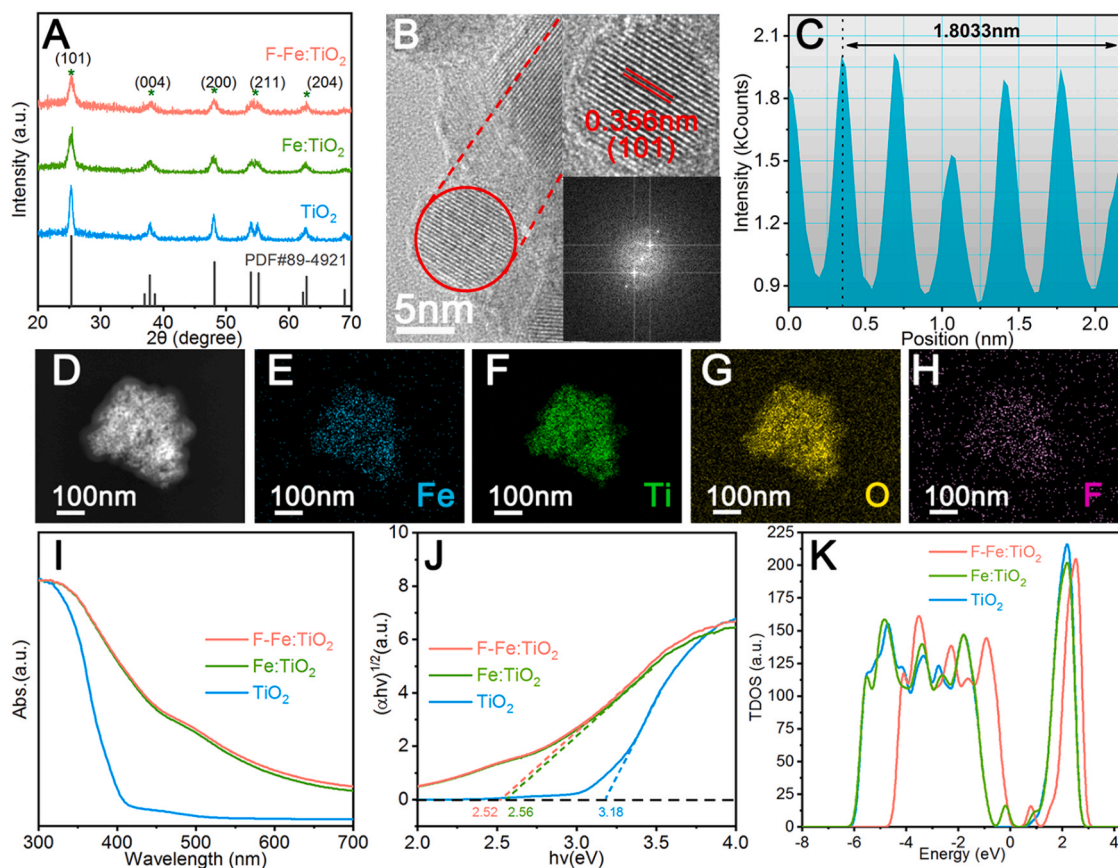


**Fig. 1.** (A) XRD patterns of pristine TiO<sub>2</sub>, Fe: TiO<sub>2</sub>, and F-Fe: TiO<sub>2</sub>. (B) HRTEM micrographs and corresponding FFT patterns of F-Fe: TiO<sub>2</sub> and (C) the interlayer spacing of F-Fe: TiO<sub>2</sub>. (D-H) SEM and EDX mapping micrographs of F-Fe: TiO<sub>2</sub>. (I) UV-vis-NIR diffuse reflectance spectroscopy and (J) the corresponding Kubelka-Munk transformed diffuse reflectance spectra of TiO<sub>2</sub>, Fe: TiO<sub>2</sub>, and F-Fe: TiO<sub>2</sub>. (K) Calculated TODS of TiO<sub>2</sub>, Fe: TiO<sub>2</sub>, and F-Fe: TiO<sub>2</sub>.

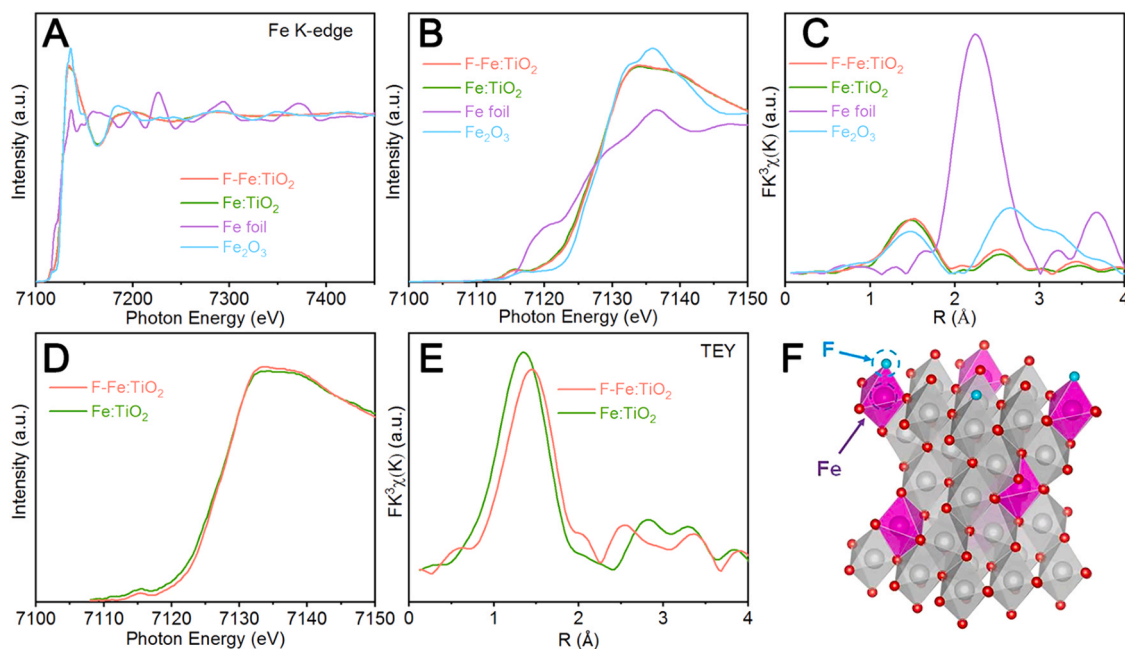


**Fig. 2.** (A) Fe K-edge XANES spectra of F-Fe: TiO<sub>2</sub> and Fe-related references. (B) Pre-edge of Fe K-edge XANES spectra. (C) The corresponding K<sub>3</sub>-weighted Fourier transform (FT) spectra in R-space. (D) Fe TEY K-edge XANES spectra of F-Fe: TiO<sub>2</sub> and Fe: TiO<sub>2</sub> and (E) The corresponding K<sub>3</sub>-weighted Fourier transform (FT) spectra in R-space. (F) Schematic diagram of F-Fe: TiO<sub>2</sub> unit cell.



TiO<sub>2</sub>, which formed the dopant energy level and the *d-d* transition of Fe species (<sup>2</sup>T<sub>2g</sub> → <sup>2</sup>A<sub>2g</sub>, <sup>2</sup>T<sub>1g</sub>). [25–27].

Density functional theory (DFT) calculations were applied to uncover the electronic structure of Fe doped and F anchored on TiO<sub>2</sub>. According to the total density of states (TDOS) calculation results in Fig. 1K, a defect level near the Fermi level is formed due to the introduction of Fe atoms, which is contributed to the extended light-harvesting in DRS UV–vis spectra and the shallow acceptor levels could promote the electron trap and transport [28]. The high electronegativity of fluorine partially replaced the surface oxygen atoms strongly attracted the electron cloud, thereby reducing the number of oxygen atoms bonded to iron atoms, which reduced the work function (W) from 5.87 eV (Fe: TiO<sub>2</sub>) to 5.35 eV (F-Fe: TiO<sub>2</sub>) as the first-principles calculations and the large effective electron mass and thereby improve the electron transport [29]. After F modification, the *d*-band center of Fe 3d shifts to higher energy, indicating a strong interaction between them and making the trap state-level position up-shift. Accordingly, the rapid dynamic of the electron transfer is driven by the large energy level transition between the trap state and the redox potential of the adsorbed N<sub>2</sub> molecules [30,31]. The above calculation predicted that Fe doped TiO<sub>2</sub> with atomical F modification could tune the surface state and upshift the trap level position, which possesses optimal electronic structure and improves the electron transport to the adsorbed N<sub>2</sub> molecules.

The X-ray absorption near-edge structure (XANES) and extended X-ray absorption fine structure (EXAFS) spectroscopy were further performed to characterize the valence state and local environment of Fe in TiO<sub>2</sub> lattice, and further verify the effect of Fe electronic state regulation in the F-Fe: TiO<sub>2</sub>. As depicted in Fig. 2A and enlarged Fig. 2B, Fe K-edge

XANES spectra of Fe: TiO<sub>2</sub> and F-Fe: TiO<sub>2</sub> presented adsorption intensity at a rising-edge position of ca. 7125 eV situated between Fe foil and Fe<sub>2</sub>O<sub>3</sub>, indicating that the mix valence state of Fe species, which was consistent with the Fe 2p XPS results. In Fig. 2C, the FT-EXAFS spectrum of F-Fe: TiO<sub>2</sub> was similar to that of Fe: TiO<sub>2</sub>, the first strong peak centered at 1.49 Å attributed to the scattering of Fe-O coordination, the smaller Fe-ligand peak located at ca. 2.5 Å further validated the formation of Fe-Ti bonds. Besides, when compared with guide Fe foil and Fe<sub>2</sub>O<sub>3</sub> samples, no significant peaks derived from Fe-Fe coordination were observed, proving the atomic dispersion of Fe into the TiO<sub>2</sub> lattice. As shown in Fig. S11, the pre-edge structure at the Ti K-edge featured three peaks: denoted as A1, A2, A3. The origin for A1 was assigned to an exciton band or a transition from 1 s → 1t<sub>g</sub> resulting from perturbation due to shake-up and shake-off process. The peak of A2 and A3 were originated from the 1 s → 3d transition and designated to 1 s → 2 t<sub>2g</sub> and 1 s → 3e<sub>g</sub> transition in an octahedral field, respectively [32]. The increased intensity of pre-edge peaks had been observed in the Fe: TiO<sub>2</sub> and F-Fe: TiO<sub>2</sub> samples comparing with pure TiO<sub>2</sub> indicating an increasing distortion from the octahedral TiO<sub>6</sub> unit, which further confirmed the Fe doping process was accompanied by the oxygen vacancy [10]. To further investigate the surface chemical state and local structure of the Fe atom before and after the fluorinated treatment, the XAFS measurement under the TEY model was carried out. As displayed in the XANES spectra of Fe K-edge (Fig. 2D), the reduced intensity of pre-edge peaks had been observed for F-Fe: TiO<sub>2</sub> compared to Fe: TiO<sub>2</sub> caused by severe Fe site distortions after the fluorinated treatment. Especially, the white line of F-Fe: TiO<sub>2</sub> was higher than that of Fe: TiO<sub>2</sub>, confirming the strong interaction between Fe and anchored F atoms. The Fe site distortion can be also testified by the FT-EXAFS spectra (Fig. 2E),

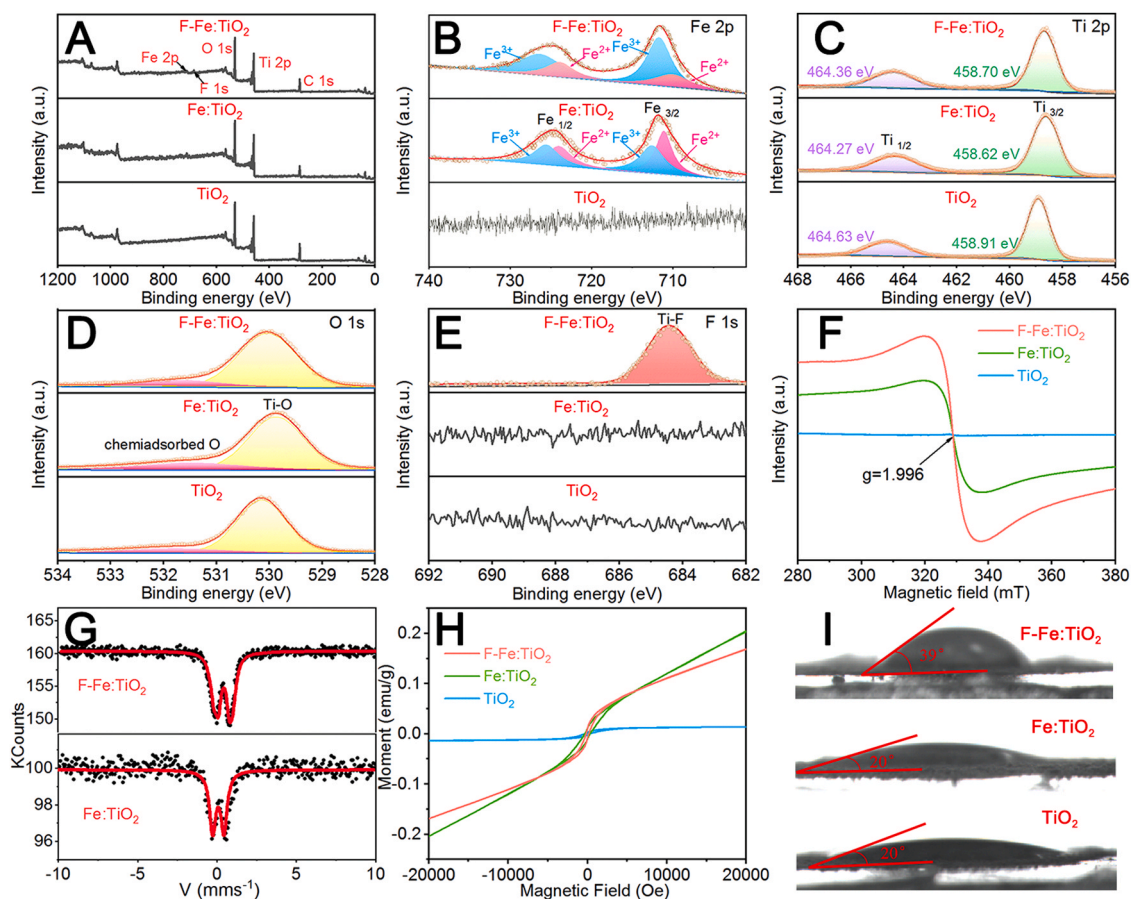


**Fig. 3.** (A) XPS survey spectra, (B) Fe 2p XPS spectra, (C) Ti 2p XPS spectra, (D) O 1s XPS spectra, (E) F 1s XPS spectra of pristine TiO<sub>2</sub>, Fe: TiO<sub>2</sub> and F-Fe: TiO<sub>2</sub>. (F) The EPR spectra of TiO<sub>2</sub>, Fe: TiO<sub>2</sub> and F-Fe: TiO<sub>2</sub>. (G) The Mössbauer spectra of Fe: TiO<sub>2</sub> and F-Fe: TiO<sub>2</sub>. (H) The M-H spectra of TiO<sub>2</sub>, Fe: TiO<sub>2</sub>, and F-Fe: TiO<sub>2</sub>. (I) Contact angle measurement of water on TiO<sub>2</sub>, Fe: TiO<sub>2</sub> and F-Fe: TiO<sub>2</sub>.

in which F-Fe: TiO<sub>2</sub> possess smaller coordination numbers and longer apical bond length than Fe: TiO<sub>2</sub>, which might be due to the regulating valence state of Fe, as the case of pressure-induced local electronic structure transition [33,34]. All the evidence indicated that Fe dopants had been successfully incorporated into TiO<sub>2</sub> lattice and simultaneously the local electronic structure of Fe sites could further be tailored by the surface anchored F atoms after the fluorinated treatment (Fig. 2F) [35].

To gain insights into the surface elemental structure and chemical valence state, the samples were identified by X-ray photoelectron spectroscopy (XPS). As the XPS full scan surveys are shown in Fig. 3A, which manifest the existence of O, Ti, and C elements in all the samples, whereas further confirmed the Fe in the Fe: TiO<sub>2</sub> and the F at the F-Fe: TiO<sub>2</sub>. The high-resolution Fe in the 2p region XPS spectrum was displayed in Fig. 3B, the doublet with the binding energy at around 724.6 and 711.5 eV could be ascribed to Fe 2p<sub>1/2</sub> and Fe 2p<sub>3/2</sub> band of Fe ions [36]. The peaks at 724.1 and 711.1 eV and 725.6 and 712.6 eV were assigned to Fe<sup>2+</sup> and Fe<sup>3+</sup>, respectively [37]. After the F modification, the peaks shift to high binding energy about 0.2 eV, and the area ratio of Fe<sup>3+</sup> to Fe<sup>2+</sup> increases from 0.9 to 2.5 compared with those of Fe: TiO<sub>2</sub>. This suggests that the electron cloud of the Fe-F bond moved to the F side as the result of F's high electronegativity. In other words, the F modification results in the increase of Fe<sup>3+</sup> on the catalyst surface. Correspondingly, the Ti 2p peaks of F-Fe: TiO<sub>2</sub> were also observed shifted to high binding energy by ~0.1 eV comparing with those of Fe: TiO<sub>2</sub> (Fig. 3C) [38]. Fig. 3D compared the O 1s XPS spectra results, it could be divided into two characteristic peaks, which from low binding energy to high binding energy were attributed to lattice oxygen (O<sub>Lat</sub>) and surface adsorbed hydroxyl oxygen (O<sub>ads</sub>), respectively [36]. Due to the replacement of Fe, displacement doping was associated with localized charge compensation and oxygen vacancies, appearing in the ratio of O<sub>ads</sub>/O<sub>Lat</sub> species slightly increased [39]. At the same time, the F signal at 684.5 eV in high-resolution F2p XPS spectra (Fig. 3E) further proves that F was successfully anchored on the F-Fe: TiO<sub>2</sub> surface.

On account of being highly sensitive to detect paramagnetic species containing Fe dopants (Fe <0.01% detectible), we also carried out the electron paramagnetic resonance (EPR) spectra to provide conclusive evidence for the lattice site in which Fe atoms were located [40]. As EPR spectra presented in Fig. 3F, the pristine TiO<sub>2</sub> sample with the almost completely paired electrons of Ti<sup>4+</sup> (3d<sup>0</sup>) displayed no intensive signal of the noise line spectra, while the Fe: TiO<sub>2</sub> and F-Fe: TiO<sub>2</sub> samples showed a very distinctive signal at g = 1.996 attributed to the partially d orbitals filled Fe(III) substituted doping in the lattice [25]. The observed broadening of the EPR signals was giving rise to the unpaired electrons of the oxygen vacancies coupled with 3d electrons of the Fe(III) sites, which confirmed the introduction of oxygen vacancies into TiO<sub>2</sub> by the Fe doping [41]. After fluorinated treatment at 400 °C, the paramagnetic signal increased dramatically, suggesting that the Fe (III) ions proportion scaled up on the surface of F-Fe: TiO<sub>2</sub>, meanwhile the rest of Fe (II) ions remained in the bulk. The above analysis of EPR results indicated that Fe cations were successfully incorporated into the crystal lattice of TiO<sub>2</sub> and a greater percentage of Fe (III) were located on the surface of F-Fe: TiO<sub>2</sub>, which agrees with XPS results.

Mossbauer spectrum was also recorded to explore the magnetization of Fe: TiO<sub>2</sub> and F-Fe: TiO<sub>2</sub> because of the electrostatic interactions between the nuclear charge and the surrounding electric charge [42]. As shown in Fig. 3G, both Fe: TiO<sub>2</sub> and F-Fe: TiO<sub>2</sub> exhibited quadrupole splitting fitted into two doublets, indicating that high-spin state Fe ions replaced Ti<sup>4+</sup> sites in an octahedral environment and no such impurities as metallic iron and iron oxides existed [43,44]. It is noteworthy that the quadrupole fitted values for the surface- fluorinated and bulk-doped Fe ions were different listed in Table S3, with an integrated area ratio of isomer shift (IS) and quadrupole splitting (QS) approached 1:1 for Fe: TiO<sub>2</sub>, revealing the defining characteristics of bulk-doped Fe(II) and surface-grafted Fe(III) [45]. In the case of F-Fe: TiO<sub>2</sub>, larger IS and QS values are corresponding to the increased Fe(III) ions with a larger structural degree of freedom after the fluorinated treatment, which was

well consistent with XPS Fe(III) and EPR results. It is widely acknowledged that Fe is a naturally magnetic element having a high ferromagnetic ordering, which is associated with the ferromagnetism in 3d transition metal oxide as the result of the mixed-valence state of Fe ions dopants [46]. To this end, a Magnetic hysteresis loop was further performed to gain in-depth structural information. Fig. 3H and S12 display the magnetization versus magnetic field (M-H) curves measured at 300 K, it could be observed an obvious ferromagnetic behavior for Fe: TiO<sub>2</sub> and F-Fe: TiO<sub>2</sub>. As listed in Table S4, the saturation magnetic field strength was 0.014, 0.101, and 0.168 emu/g for the TiO<sub>2</sub>, Fe: TiO<sub>2</sub>, and F-Fe: TiO<sub>2</sub> samples, respectively. In this work, this was due to the balance principle between the creation of charge compensating and the density of bound magnetic polarons (BMPs) coupling mediated by the shallow donor electrons (trapped by Fe dopants or oxygen vacancies) and overlapped a spin-spin impurity band by the surficial effects after the fluorinated treatment [47,48]. Fig. 3I displays the contact angle images of TiO<sub>2</sub>, Fe: TiO<sub>2</sub>, and F-Fe: TiO<sub>2</sub> samples. The contact angle increased from ~20 to ~39 degrees before and after F modification illustrating that the F-Fe: TiO<sub>2</sub> sample had better hydrophobic properties. The increasing contact angle may be caused by the capping of F on the surface. Providing high N<sub>2</sub> concentration on the electrode surface via surface modification turns to be a critical issue for eNRR. The eNRR process carries out at three-phase interfaces in an aqueous solution, which includes N<sub>2</sub> in gas, H<sub>2</sub>O in liquid, and electrode in the solid phase, therefore the low solubility of N<sub>2</sub> (20 mg L<sup>-1</sup>) and competitive HER hinder the efficiency of eNRR. The surface wettability change of catalyst may minimize direct proton adsorption and promote N<sub>2</sub> molecules adsorption during the electroreduction reaction to boost the productivity of the NH<sub>3</sub> evolution process, as well.

### 3.2. Electrocatalytic activity

The electrocatalytic activities of the catalysts were evaluated by the quantification of NH<sub>3</sub>(aq.)/NH<sub>4</sub><sup>+</sup> in a three-electrode H-cell electrochemical system at controllable applied voltages. The feeding gas was purified by 2 M NaOH, 0.1 M FeSO<sub>4</sub>, and 5 mM H<sub>2</sub>SO<sub>4</sub> solutions to exclude the possible interferences of NH<sub>3</sub> and NO<sub>x</sub>. [49] The catalysts were loaded on 1 × 1 cm<sup>2</sup> carbon paper as the working electrode for comparison. All reported potentials were recorded with respect to a reversible hydrogen electrode (RHE) scale. The NH<sub>4</sub><sup>+</sup>-containing products were qualitative and quantitatively analyzed by ion chromatography. As shown in Fig. 4A, the linear sweep voltammetry (LSV) curve of Fe: TiO<sub>2</sub> and F-Fe: TiO<sub>2</sub> were measured under N<sub>2</sub>-bubbled electrolytes with TiO<sub>2</sub> as a comparison. The observed current density of F-Fe: TiO<sub>2</sub> is higher than the catalysts indicating a higher NRR activity. That suggests that Fe dopants and surface F modification have the largest interfacial reaction kinetics to promote the NRR catalysis. The corresponding Tafel slope of 85.87 mV dec<sup>-1</sup> derived from F-Fe: TiO<sub>2</sub> is much smaller than TiO<sub>2</sub> (175.13 mV dec<sup>-1</sup>) and Fe: TiO<sub>2</sub> (123.07 mV dec<sup>-1</sup>), revealing the significantly accelerated first electron-transfer step (\*N<sub>2</sub> + e<sup>-</sup> + H → \*NNH) which is consistent with the calculated rate-limiting step in Fig. 4B. In addition, the electrochemical adsorption capability of catalysis was quantitatively analyzed by double-layer capacitances (Fig. S13) [50], the calculated electrochemical active surface areas (ECSAs) of F-Fe: TiO<sub>2</sub> was 287.1 cm<sup>2</sup>. The corresponding electrochemical impedance spectrum (EIS) was carried out and the Nyquist plot and the equivalent circuit were also shown in Fig. 4C. The corresponding fitting resistances and capacitors are listed in Table S5. On account of the minimum arc radius (R<sub>ct</sub> values) for F-Fe: TiO<sub>2</sub>, implying the F-Fe: TiO<sub>2</sub> catalyst had the lowest resistance and highest electron transfer efficiency. We further examined the NRR performance of F-Fe: TiO<sub>2</sub> under different applied voltages, as displayed in Fig. 4D, revealing the highest NH<sub>3</sub> production is achieved at -0.5 V vs RHE. The corresponding highest Faradaic efficiency (FE) and maximum NH<sub>3</sub> production rate were 27.67% and 27.86 μg h<sup>-1</sup> mg<sub>cat</sub><sup>-1</sup>, which are about 5 folds better than those of TiO<sub>2</sub>, respectively. When the applied potential continued

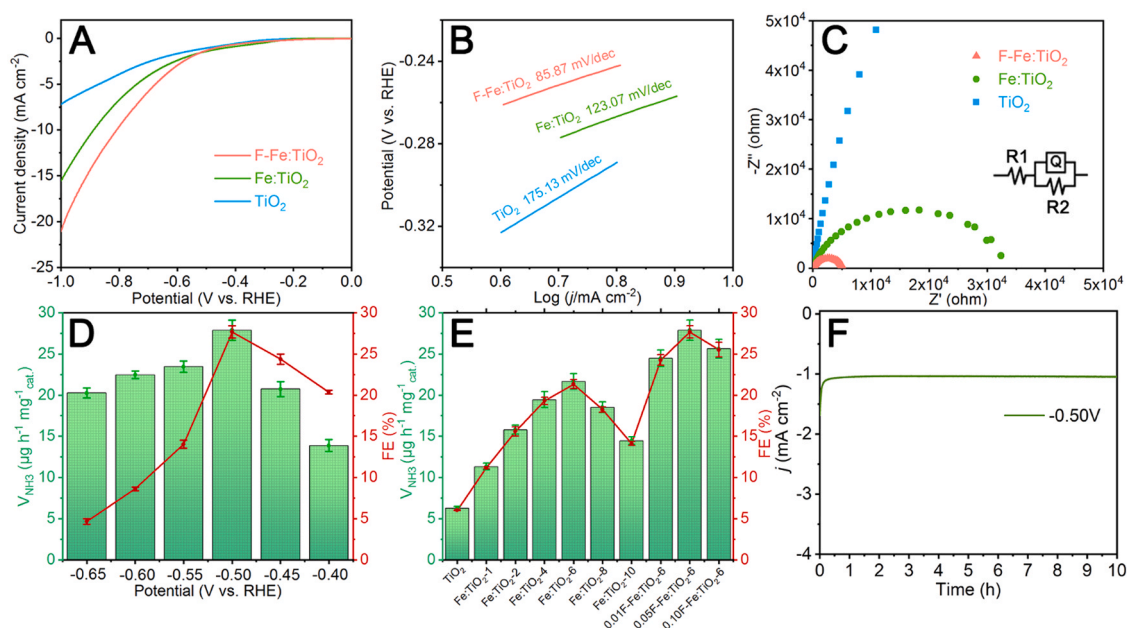


**Fig. 4.** (A) The LSV curves under the  $N_2$  atmosphere and (B) the corresponding Tafel slope, (C) EIS spectra of pristine  $TiO_2$ ,  $Fe:TiO_2$ , and  $F-Fe:TiO_2$ , (D) FEs and  $NH_3$  yields over  $F-Fe:TiO_2$  at various potentials. (E) FEs and  $NH_3$  yield over different samples at  $-0.50$  V for 2 h. (F) Time-dependent current density curves of  $F-Fe:TiO_2$  under  $-0.50$  V in  $N_2$ -saturated  $0.05$  M  $H_2SO_4$  for 7200 s.

to increase, the  $NH_3$  production rate and FE were decreased, mainly owing to the dominant of the competitive HER process. Considering both Fe dopants and fluorinated treatment had great influences on enhancing NRR performance, a series of optimization experiments were carried out in Fig. 4E. It is noteworthy that there was a typical volcano plot along the Fe doping and F treating dose, which demonstrated that excess dose may hinder the electrons transfer in bulk and interface result in the subsequent inactivation of NRR performance.

To further identify the origin of produced  $NH_3$  from the electrocatalytic N elements conversion, the  $^{15}N$  isotopic labeling experiment was performed by using  $^{14}N_2$  and  $^{15}N_2$  as feeding gas, respectively. Because of the quadrupole moment of N, the H adjacent to the  $^{14}N$  splits into triple peaks,  $^{15}N$  exhibited distinguishable doublet coupling peaks by contrast, as the  $^1H$  nuclear magnetic resonance (NMR) spectra shown in Fig. S14. That implies that the nitrogen comes from  $N_2$  in  $NH_3$  production. Generally, the hydrogen evolution reaction (HER) is competitive [51]. Fig. S15 displays the LSV curves of  $F-Fe:TiO_2$  under  $N_2$  and Ar-bubbled reaction. It exhibits low over-potential and high current density at the same potential for the  $N_2$  saturated reaction indicating that NRR happens more easily in  $N_2$  saturated reaction than that in Ar saturated reaction.

To verify the stability of catalyst, the chronoamperometric (i-t) curves of  $F-Fe:TiO_2$  are presented in Fig. 4F, the current density had not decreased within 7000 s, indicating that the  $F-Fe:TiO_2$  catalyst had favorable recycling ability, good activity, and stability. In addition, the XRD, TEM, and XPS results of  $F-Fe:TiO_2$  were performed after the NRR experiment are presented in Figs. S16-S18. There is no significant difference after the long-term reaction, further confirming the excellent stability of  $F-Fe:TiO_2$ .

### 3.3. Identification of NRR catalytic sites

To support the experimental data to investigate the NRR mechanism, density functional theory (DFT) calculations were carried out by using Perdew–Burke–Ernzerhof (PBE) generalized gradient approximation and the projected augmented wave (PAW) method implemented in the VASP package. In all the calculations, the cutoff energy for the plane-wave basis was set at 400 eV. The criteria for energy is set as  $10^{-4}$  eV

and for residual force is  $0.01$  eV  $\text{\AA}^{-1}$ . The predominant  $TiO_2$  (101) facet as determined by XRD/HRTEM was selected for slab modeling. The  $TiO_2$  (101) surface slab in the  $Ti_{48}O_{96}$  formula was constructed with eight atomic layers and the lateral size of  $a = 10.226$   $\text{\AA}$ ,  $b = 11.408$   $\text{\AA}$ . Moreover, a vacuum with a thickness of 15  $\text{\AA}$  was employed perpendicular to the slab to eliminate interaction between adjacent images. DFT calculation results suggested that  $N_2$  molecule can preferentially adsorb on low-coordinate surface terminated Fe atom by end-on configuration with a high adsorption energy of  $-0.19$  eV (Fig. 5A) compared with  $-0.13$  eV adsorption energy for pure  $TiO_2$ . Moreover, Bader charge analysis indicated that 0.017 e was transferred into  $N_2$  molecules, such as electron accumulation (yellow shadow) and depletion (cyan shadow) observed in Fig. 5B. In the case of  $F-Fe:TiO_2$ , the electronegative F atom may occupy the concomitant Ov site or cap on the  $Fe:TiO_2$  surface after the fluorinated treatment. The N-N bond of adsorbed  $N_2$  was lengthened to 1.122  $\text{\AA}$  and the corresponding adsorption energy increased to  $-0.4$  eV in comparison with that of the  $N_2$  molecule adsorbed on  $Fe:TiO_2$  (Fig. 5C). Besides, the charge density differences for  $F-Fe:TiO_2$  with the adsorbed  $N_2$  molecule and electron enrichment between N and surface Ti atoms in Fig. 5D, and the Bader charge analysis showed that 0.032 e was transferred into  $N_2$  molecule, which was much higher than those of  $Fe:TiO_2$ . Therefore, it was evident from these results that the efficiently 3d electrons donated from surface-active Fe sites to the antibonding  $1\pi^*$  orbital of adsorbed  $N_2$  ( $*N_2$ ), which led to the polarize and activate of the inert triple bonded  $N_2$  [52]. In the generally accepted reaction pathways of  $N_2$  reduction to  $NH_3$  depending on the end-on adsorption modes of  $N_2$  molecules, hydrogen atoms were added one by one to adsorbed  $N_2$  [53]. To acquire free energy profiles, the computational electrode model (CHE) was applied [53, 54]. Fig. 5E depicted local atomic structures of the reaction intermediates and the free energy diagram of the NRR pathways. Given the high  $NH_3$  solubility promoting the release of the first and second generated  $*NH_3$ , the first hydrogenation step forming  $NNH^*$  was considered as the rate-determining step in the whole  $N_2$  fixation process, which required an uphill 0.79 eV reaction energy in concert with the previous literature [55,56]. Furthermore, after applying an external potential of  $U = -0.5$  V determined by the electrocatalytic results, the RDS barrier was corresponding reduced and the whole NRR process



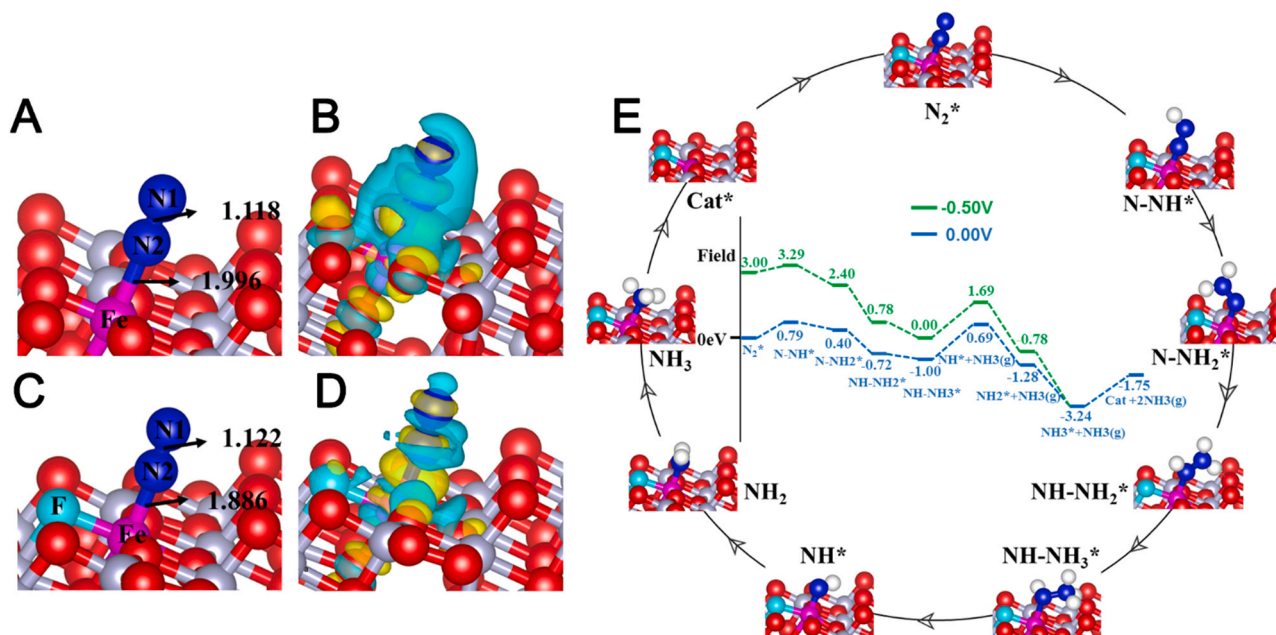


**Fig. 5.** (A, C) Atom configurations of optimized adsorption configuration for N<sub>2</sub> over Fe: TiO<sub>2</sub> and F-Fe: TiO<sub>2</sub> (101) surface. Light gray, red, cyan, purple, and blue balls denote Ti, O, F, Fe, and N atoms, respectively. (B, D) Charge density difference plots of N<sub>2</sub> adsorption over Fe: TiO<sub>2</sub> and F-Fe: TiO<sub>2</sub> (101) surface. The blue (yellow) wireframes denote the loss (gain) of electrons. (E) Calculated free energy diagram for hydrogenation steps at  $U = -0.50$  V for adsorbed N<sub>2</sub> over F-Fe: TiO<sub>2</sub> (101) surface and corresponding atom configurations.

tended to be spontaneous proceed. Based on the above calculation and analysis results, it can be predicted that incorporation of Fe dopants into TiO<sub>2</sub> (101) surface proven as effective active centers, and the multi-step optimized F-Fe: TiO<sub>2</sub> further modulated local electronic structure, which had potentially superior catalytic activity for the N<sub>2</sub>-to-NH<sub>3</sub> conversion.

#### 4. Conclusions

In summary, we synthesized the surface F modified Fe doped TiO<sub>2</sub> electrocatalyst for N<sub>2</sub> electroreduction. Fe dopants in TiO<sub>2</sub> induced oxygen vacancies by the localized charge compensation and a defect energy level below the conduction band enhanced N<sub>2</sub> adsorption. After the surface fluorine modification, the surface electric state is tuned to up-shift and the dopant tends to be high spin state Fe(III). Those promote electron transfer from the d-electrons of the Fe to the N 1 $\pi$ g\* orbital through backdonation. Also, the orbital hybridization of Fe 3d and F 2p with electron delocalization lowers the energy barrier of the rate-limiting step for N<sub>2</sub> electroreduction into NH<sub>3</sub>. Consequently, the optimal F-Fe: TiO<sub>2</sub> electrocatalyst achieved the highest faradaic efficiency (FE) and maximum NH<sub>3</sub> production rate of 27.67% and 27.86  $\mu\text{g h}^{-1} \text{mg}_{\text{cat}}^{-1}$  at  $-0.5$  V versus RHE, which was approximately 5 times as high as that (4.8%) of pristine TiO<sub>2</sub>. This work provides a facile way to regulate the surface electronic state of Fe ions in TiO<sub>2</sub> and sheds a light on multi-step optimization of electrocatalyst toward N<sub>2</sub> efficient fixation.

#### Author contributions

The manuscript was written through the contributions of all authors. All authors have approved the final version of the manuscript.

#### CRediT authorship contribution statement

**Guangxin Song:** Investigation, **Rui Gao:** Validation, **Zhao Zhao:** Conceptualization, Methodology, Writing – original & draft, **Yujun Zhang:** Resources, **Huaqiao Tan:** Conceptualization, **Haibo Li:** Funding acquisition, Supervision, **Dandan Wang:** Methodology, **Zaicheng Sun:**

Conceptualization, Methodology, Writing – review & editing. **Ming Feng:** Funding acquisition, Resources and Validation.

#### Declaration of Competing Interest

The authors declare that they have no known competing financial interests or personal relationships that could have appeared to influence the work reported in this paper.

#### Acknowledgment

This work is financially supported by the National Natural Science Foundation of China (Grant Nos. 21801092, 21872001, 21978110, 51772126, and 52171210), the Program for the Development of Science and Technology of Jilin Province (Item Nos. 20200201187JC and 20200801040GH), the Science and Technology Project of the “13th Five-Year Plan” of Jilin Provincial Education Department (Nos. JJKH20200406KJ and JJKH20200407KJ), the Jilin Province Development and Reform Commission Program (No. 2020C026–3), the Fundamental Research Funds for the Central Universities (Grant Nos. 2412018BJ001 and 2412018ZD007), and the “Hong Kong Scholar” program (Grant No. XJ2018021). Allocation of beamtime at 1W1B and 4B9B beamline, BSRF, Beijing, China, is gratefully acknowledged.

#### Appendix A. Supporting information

Supplementary data associated with this article can be found in the online version at [doi:10.1016/j.apcatb.2021.120809](https://doi.org/10.1016/j.apcatb.2021.120809).

#### References

- [1] D. Hao, Y. Liu, S. Gao, H. Arandian, X. Bai, Q. Kong, W. Wei, P.K. Shen, B.-J. Ni, Emerging artificial nitrogen cycle processes through novel electrochemical and photochemical synthesis, *Mater. Today* 46 (2021) 212–233.
- [2] X. Yang, F. Ling, J. Su, X. Zi, H. Zhang, H. Zhang, J. Li, M. Zhou, Y. Wang, Insights into the role of cation vacancy for significantly enhanced electrochemical nitrogen reduction, *Appl. Catal. B Environ.* 264 (2020), 118477.
- [3] G. Ertl, Reactions at surfaces: from atoms to complexity (Nobel Lecture), *Angew. Chem. Int. Ed. Engl.* 47 (2008) 3524–3535.

- [4] H. Liu, Ammonia synthesis catalyst 100 years: practice, enlightenment and challenge, *Chin. J. Catal.* 35 (2014) 1619–1640.
- [5] L. Niu, L. An, X. Wang, Z. Sun, Effect on electrochemical reduction of nitrogen to ammonia under ambient conditions: Challenges and opportunities for chemical fuels, *J. Energy Chem.* 61 (2021) 304–318.
- [6] Z.-Y. Pan, Z. Tang, Y.-Z. Zhan, D. Sun, Three-dimensional porous CoNiO<sub>2</sub>@reduced graphene oxide nanosheet arrays/nickel foam as a highly efficient bifunctional electrocatalyst for overall water splitting, *Tungsten* 2 (2020) 390–402.
- [7] L. Shi, Y. Yin, S. Wang, X. Xu, H. Wu, J. Zhang, S. Wang, H. Sun, Rigorous and reliable operations for electrocatalytic nitrogen reduction, *Appl. Catal. B Environ.* 278 (2020), 119325.
- [8] R. Manjunatha, A. Karajić, M. Liu, Z. Zhai, L. Dong, W. Yan, D.P. Wilkinson, J. Zhang, A review of composite/hybrid electrocatalysts and photocatalysts for nitrogen reduction reactions: advanced materials, mechanisms, challenges and perspectives, *Electrochem. Energy Rev.* 3 (2020) 506–540.
- [9] Y. Yao, J. Wang, U.B. Shahid, M. Gu, H. Wang, H. Li, M. Shao, Electrochemical synthesis of ammonia from nitrogen under mild conditions: current status and challenges, *Electrochem. Energy Rev.* 3 (2020) 239–270.
- [10] Z. Han, C. Choi, S. Hong, T.-S. Wu, Y.-L. Soo, Y. Jung, J. Qiu, Z. Sun, Activated TiO<sub>2</sub> with tuned vacancy for efficient electrochemical nitrogen reduction, *Appl. Catal. B: Environ.* 257 (2019), 117896.
- [11] Q. Liu, T. Xu, Y. Luo, Q. Kong, T. Li, S. Lu, A.A. Alshehri, K.A. Alzahrani, X. Sun, Recent advances in strategies for highly selective electrocatalytic N<sub>2</sub> reduction toward ambient NH<sub>3</sub> synthesis, *Curr. Opin. Electrochem.* 29 (2021), 100766.
- [12] M. Zhang, Z. Wang, H. Yu, S. Wang, Y. Xu, X. Li, L. Wang, H. Wang, A mesoporous Au film with surface sulfur modification for efficient ammonia electrosynthesis, *J. Mater. Chem. A* 8 (2020) 20414–20419.
- [13] J. Wang, L. Yu, L. Hu, G. Chen, H. Xin, X. Feng, Ambient ammonia synthesis via palladium-catalyzed electrohydrogenation of dinitrogen at low overpotential, *Nat. Commun.* 9 (2018) 1795.
- [14] H. Zhao, D. Zhang, Z. Wang, Y. Han, X. Sun, H. Li, X. Wu, Y. Pan, Y. Qin, S. Lin, Z. Xu, J. Lai, L. Wang, High-performance nitrogen electroreduction at low overpotential by introducing Pb to Pd nanosponges, *Appl. Catal. B Environ.* 265 (2020), 118481.
- [15] Y. Yao, H. Wang, X.-z. Yuan, H. Li, M. Shao, Electrochemical nitrogen reduction reaction on ruthenium, *ACS Energy Lett.* 4 (2019) 1336–1341.
- [16] C. Guo, X. Liu, L. Gao, X. Kuang, X. Ren, X. Ma, M. Zhao, H. Yang, X. Sun, Q. Wei, Fe-doped Ni<sub>2</sub>P nanosheets with porous structure for electroreduction of nitrogen to ammonia under ambient conditions, *Appl. Catal. B Environ.* 263 (2020), 118296.
- [17] T. Xu, B. Ma, J. Liang, L. Yue, Q. Liu, T. Li, H. Zhao, Y. Luo, S. Lu, X. Sun, Recent progress in metal-free electrocatalysts toward ambient N<sub>2</sub> reduction reaction, *Acta Phys. Chim. Sin.* 0 (2020), 2009043-2009040.
- [18] B. Ma, H. Zhao, T. Li, Q. Liu, Y. Luo, C. Li, S. Lu, A.M. Asiri, D. Ma, X. Sun, Iron-group electrocatalysts for ambient nitrogen reduction reaction in aqueous media, *Nano Res.* 14 (2020) 555–569.
- [19] W. Zhao, J. Zhang, X. Zhu, M. Zhang, J. Tang, M. Tan, Y. Wang, Enhanced nitrogen photofixation on Fe-doped TiO<sub>2</sub> with highly exposed (101) facets in the presence of ethanol as scavenger, *Appl. Catal. B Environ.* 144 (2014) 468–477.
- [20] C. Fang, W. An, Single-metal-atom site with high-spin state embedded in defective BN nanosheet promotes electrocatalytic nitrogen reduction, *Nano Res.* (2021) 1–9.
- [21] X. Li, X. Wu, S. Liu, Y. Li, J. Fan, K. Lv, Effects of fluorine on photocatalysis, *Chin. J. Catal.* 41 (2020) 1451–1467.
- [22] R. Fu, Z. Wu, Z. Pan, Z. Gao, Z. Li, X. Kong, L. Li, Fluorine-induced surface metallization for ammonia synthesis under photoexcitation up to 1550 nm, *Angew. Chem. Int. Ed. Engl.* 60 (2021) 11173–11179.
- [23] X. Cheng, J. Wang, W. Xiong, T. Wang, T. Wu, S. Lu, G. Chen, S. Gao, X. Shi, Z. Jiang, X. Niu, X. Sun, Greatly enhanced electrocatalytic N<sub>2</sub> reduction over V<sub>2</sub>O<sub>3</sub>/C by P doping, *ChemNanoMat* 6 (2020) 1315–1319.
- [24] Z. Huang, Y. Zhang, Y. He, H. Song, C. Yin, K. Wu, A chemist's overview of surface electron spins, *Chem. Soc. Rev.* 46 (2017) 1955–1976.
- [25] Y. Niu, M. Xing, J. Zhang, B. Tian, Visible light activated sulfur and iron co-doped TiO<sub>2</sub> photocatalyst for the photocatalytic degradation of phenol, *Catal. Today* 201 (2013) 159–166.
- [26] K. Nagaveni, M.S. Hegde, G. Madras, Structure and photocatalytic activity of Ti<sub>1-x</sub>M<sub>x</sub>O<sub>2</sub> +/-delta (M = W, V, Ce, Zr, Fe, and Cu) synthesized by solution combustion method, *J. Phys. Chem. B* 108 (2004) 20204–20212.
- [27] J. Zhu, F. Chen, J. Zhang, H. Chen, M. Anpo, Fe<sup>3+</sup>-TiO<sub>2</sub> photocatalysts prepared by combining sol-gel method with hydrothermal treatment and their characterization, *J. Photochem. Photo A Chem.* 180 (2006) 196–204.
- [28] J. Ma, H. He, F. Liu, Effect of Fe on the photocatalytic removal of NO over visible light responsive Fe/TiO<sub>2</sub> catalysts, *Appl. Catal. B Environ.* 179 (2015) 21–28.
- [29] H. Peng, S. Lany, Semiconducting transition-metal oxides based on dScations: theory for MnO and Fe<sub>2</sub>O<sub>3</sub>, *Phys. Rev. B* 85 (2012), 201202.
- [30] J. Zhang, R. García-Rodríguez, P. Cameron, S. Eslava, Role of cobalt-iron (oxy) hydroxide (CoFeO<sub>x</sub>) as oxygen evolution catalyst on hematite photoanodes, *Energy Environ. Sci.* 11 (2018) 2972–2984.
- [31] S. Chen, J. Bai, X. Nurimaimaiti, J. Wang, Y. Zhang, T. Zhou, J. Li, B. Zhou, Surface metal valence state regulating on hematite to weaken dependence of charge transport to catalyst loading, *Nano Energy* 78 (2020), 105396.
- [32] N. Jiang, D. Su, J.C.H. Spence, Determination of Ti coordination from pre-edge peaks in TiK-edge XANES, *Phys. Rev. B* 76 (2007), 214117.
- [33] Y. Bo, H. Wang, Y. Lin, T. Yang, R. Ye, Y. Li, C. Hu, P. Du, Y. Hu, Z. Liu, R. Long, C. Gao, B. Ye, L. Song, X. Wu, Y. Xiong, Altering hydrogenation pathways in photocatalytic nitrogen fixation by tuning local electronic structure of oxygen vacancy with dopant, *Angew. Chem. Int. Ed. Engl.* 60 (2021) 16085–16092.
- [34] Y. Liu, C. Xiao, P. Huang, M. Cheng, Y. Xie, Regulating the charge and spin ordering of two-dimensional ultrathin solids for electrocatalytic water splitting, *Chem* 4 (2018) 1263–1283.
- [35] R. Guan, D. Wang, Y. Zhang, C. Liu, W. Xu, J. Wang, Z. Zhao, M. Feng, Q. Shang, Z. Sun, Enhanced photocatalytic N<sub>2</sub> fixation via defective and fluoride modified TiO<sub>2</sub> surface, *Appl. Catal. B Environ.* 282 (2021), 119580.
- [36] T. Yamashita, P. Hayes, Analysis of XPS spectra of Fe<sup>2+</sup> and Fe<sup>3+</sup> ions in oxide materials, *Appl. Surf. Sci.* 254 (2008) 2441–2449.
- [37] X. Huang, M. Lu, X. Zhang, G. Wen, Y. Zhou, L. Fei, Carbon microtube/Fe<sub>3</sub>O<sub>4</sub> nanocomposite with improved wave-absorbing performance, *Scr. Mater.* 67 (2012) 613–616.
- [38] H. Chen, J. Liang, L. Li, B. Zheng, Z. Feng, Z. Xu, Y. Luo, Q. Liu, X. Shi, Y. Liu, S. Gao, A.M. Asiri, Y. Wang, Q. Kong, X. Sun, Ti<sub>2</sub>O<sub>3</sub> nanoparticles with Ti(3+) sites toward efficient NH<sub>3</sub> electrosynthesis under ambient conditions, *ACS Appl. Mater. Interfaces* 13 (2021) 41715–41722.
- [39] S. Gong, Z. Xie, W. Li, X. Wu, N. Han, Y. Chen, Highly active and humidity resistive perovskite LaFeO<sub>3</sub> based catalysts for efficient ozone decomposition, *Appl. Catal. B Environ.* 241 (2019) 578–587.
- [40] J. Zhu, W. Zheng, B. He, J. Zhang, M. Anpo, Characterization of Fe-TiO<sub>2</sub> photocatalysts synthesized by hydrothermal method and their photocatalytic reactivity for photodegradation of XRG dye diluted in water, *J. Mol. Catal. A Chem.* 216 (2004) 35–43.
- [41] C. Adán, A. Bahamonde, M. Fernández-García, A. Martínez-Arias, Structure and activity of nanosized iron-doped anatase TiO<sub>2</sub> catalysts for phenol photocatalytic degradation, *Appl. Catal. B Environ.* 72 (2007) 11–17.
- [42] J.-M.M. Millet, Mössbauer Spectrosc. Heterog. Catal. (2007) 309–350.
- [43] M. Liu, X. Qiu, M. Miyauchi, K. Hashimoto, Energy-level matching of Fe(III) ions grafted at surface and doped in bulk for efficient visible-light photocatalysts, *J. Am. Chem. Soc.* 135 (2013) 10064–10072.
- [44] F. Lin, D. Jiang, Y. Lin, X. Ma, Magnetism of Fe-doped TiO<sub>2</sub> milled in different milling atmospheres, *Phys. B Condens Matter* 403 (2008) 2193–2196.
- [45] H.M. Lee, C.S. Kim, Effects of oxygen vacancies on the ferromagnetism in Fe-doped anatase TiO<sub>2</sub>, *J. Magn. Magn. Mater.* 310 (2007) 2099–2101.
- [46] P. Xiaoyan, J. Dongmei, L. Yan, M. Xueming, Structural characterization and ferromagnetic behavior of Fe-doped TiO<sub>2</sub> powder by high-energy ball milling, *J. Magn. Magn. Mater.* 305 (2006) 388–391.
- [47] M. Nageri, V. Kumar, Manganese-doped BaTiO<sub>3</sub> nanotube arrays for enhanced visible light photocatalytic applications, *Mater. Chem. Phys.* 213 (2018) 400–405.
- [48] J.M. Coey, M. Venkatesan, C.B. Fitzgerald, Donor impurity band exchange in dilute ferromagnetic oxides, *Nat. Mater.* 4 (2005) 173–179.
- [49] L. Han, X. Liu, J. Chen, R. Lin, H. Liu, F. Lu, S. Bak, Z. Liang, S. Zhao, E. Stavitski, J. Luo, R.R. Adzic, H.L. Xin, Atomically dispersed molybdenum catalysts for efficient ambient nitrogen fixation, *Angew. Chem. Int. Ed. Engl.* 58 (2019) 2321–2325.
- [50] C. Huang, L. Shang, P. Han, Z. Gu, A.M. Al-Enizi, T.M. Almutairi, N. Cao, G. Zheng, Electrochemical N<sub>2</sub> fixation by Cu-modified iron oxide dendrites, *J. Colloid Interface Sci.* 552 (2019) 312–318.
- [51] T. Xu, J. Liang, Y. Wang, S. Li, Z. Du, T. Li, Q. Liu, Y. Luo, F. Zhang, X. Shi, B. Tang, Q. Kong, A.M. Asiri, C. Yang, D. Ma, X. Sun, Enhancing electrocatalytic N<sub>2</sub>-to-NH<sub>3</sub> fixation by suppressing hydrogen evolution with alkylthiols modified Fe<sub>3</sub>P nanoarrays, *Nano Res.* (2021) 1–8.
- [52] X.F. Li, Q.K. Li, J. Cheng, L.L. Liu, Q. Yan, Y.C. Wu, X.H. Zhang, Z.Y. Wang, Q. Qiu, Y. Luo, Conversion of dinitrogen to ammonia by FeN<sub>3</sub>-embedded graphene, *J. Am. Chem. Soc.* 138 (2016) 8706–8709.
- [53] H. Li, J. Shang, Z. Ai, L. Zhang, Efficient visible light nitrogen fixation with BiOBr nanosheets of oxygen vacancies on the exposed {001} facets, *J. Am. Chem. Soc.* 137 (2015) 6393–6399.
- [54] H. Yang, D. Luo, R. Gao, D. Wang, H. Li, Z. Zhao, M. Feng, Z. Chen, Reduction of N<sub>2</sub> to NH<sub>3</sub> by TiO<sub>2</sub>-supported Ni cluster catalysts: a DFT study, *Phys. Chem. Chem. Phys.* 23 (2021) 16707–16717.
- [55] Z. Wang, F. Gong, L. Zhang, R. Wang, L. Ji, Q. Liu, Y. Luo, H. Guo, Y. Li, P. Gao, X. Shi, B. Li, B. Tang, X. Sun, Electrocatalytic hydrogenation of N<sub>2</sub> to NH<sub>3</sub> by MnO: experimental and theoretical investigations, *Adv. Sci. (Weinh.)* 6 (2019), 1801182.
- [56] L. Zhang, X. Ji, X. Ren, Y. Ma, X. Shi, Z. Tian, A.M. Asiri, L. Chen, B. Tang, X. Sun, Electrochemical ammonia synthesis via nitrogen reduction reaction on a MoS<sub>2</sub> catalyst: theoretical and experimental studies, *Adv. Mater.* 30 (2018), e1800191.